Coupled Multiphase Fluid Flow and Wellbore Stability Analysis Associated with Gas Production from Oceanic Hydrate-Bearing Sediments

J. Rutqvist[1,] *, G.J. Moridis[1], T. Grover[2,Ψ], S. Silpngarmlert[3], T.S. Collett[4], S.A. Holdich[2]

[1]*Earth Sciences Division, Lawrence Berkeley National Laboratory, MS 90-1116, Berkeley, CA 947 20, USA*

[2]*Petroleum Engineering Department, Texas A&M University, MS 3116, Richardson Building, College Station, TX, 77843, USA*

[3]*ConocoPhillips, P.O. Box 2197, Houston, TX 77252*

[4]*U.S. Geological Survey, Denver Federal Center, Box 25046, MS-939, Denver, CO 80225, USA*

* Corresponding author. Tel.: +1-510-486-5432, fax.: +1-510-486-5686
e-mail address: jrutqvist@lbl.gov (J. Rutqvist)

[Ψ]*Now with StatoilHydro ASA, Technology and New Energy – Production Technology, 4035 Stavanger, Norway*

Submitted to Journal of Petroleum Sciences and Engineering (2012)

ABSTRACT

We conducted numerical modeling of coupled multiphase fluid-flow, thermal, and geomechanical processes during gas production from an oceanic hydrate deposit to study the geomechanical performance and wellbore stability. We investigated two alternative cases of depressurization-induced gas production: (1) production from horizontal wells in a Class 3 deposit (a hydrate layer sandwiched between two low-permeability layers), and (2) production from vertical wells in a Class 2 deposit (a hydrate layer with an underlying zone of mobile water). The analysis showed that geomechanical responses around the wellbore are driven by reservoir-wide pressure depletion, which in turn, depends on production rate and pressure decline at the wellbore. The calculated vertical compaction of the relatively soft sediments and increased shear stress caused local yielding of the formation around the well assembly for both the horizontal and vertical well cases. However, the analysis also showed that the extent of the yield zone can be reduced if using overbalanced drilling (at an internal well pressure above the formation fluid pressure) and well completion that minimizes any annular gap between the well assembly and the formation. Our further analysis indicated that the most extensive yield zone would occur around the perforated production interval of a vertical well, where the pressure gradient is the highest. In the field, such yielding and shearing of the sediments could lead to enhanced sand production if not prevented with appropriate sand control technology. Moreover, our analysis shows that the vertical compaction of the reservoir can be substantial, with subsidence on the order of several meters and vertical compaction strain locally exceeding 10%. In the field, such substantial compaction strain will require appropriate well design (such as slip joints or heavy wall casing) to avoid tensile or buckling failure of the well assembly.

Keywords: hydrates, geomechanics, modeling, well stability, gas production, subsidence

NOMENCLATURE

BPD = barrels per day
C = specific heat (J/kg/K)
C_m = cohesion (Pa)
G = shear modulus of elasticity (Pa)
k = intrinsic permeability (m^2)
k_{eff} = effective permeability = $k\,k_{r\beta}$ (m^2)
$k_{r\beta}$ = relative permeability of phase β (= A, G, H)
k_Θ = thermal conductivity (W/m/K)
$k_{\Theta RD}$ = thermal conductivity of dry porous medium (W/m/K)
$k_{\Theta RW}$ = thermal conductivity of fully saturated porous medium (W/m/K)
K = bulk modulus of elasticity (Pa)
N_H = hydration number
P = pressure (Pa)
P_c = capillary pressure (Pa)
P_w = constant well pressure (Pa)
Q = volumetric rate (ST m^3/s)
Q_w = water mass production rate (kg/s)
R_{CWG} = cumulative water-to-gas ratio (kg/ST m^3)
x,r,y,z = coordinates (m)
S_β = saturation of phase β (= A, G, H)
t = time (days)
T = temperature (K or ^oC)

Greek Symbols

α = Pore compressibility (Pa^{-1})
ε = strain
λ = van Genuchten exponent – Table 2
μ = coefficient of internal friction
σ = stress (Pa)
σ' = effective stress (Pa)
ϕ = porosity

Subscripts and Superscripts

0 = denotes initial state
A = aqueous phase
B = base of HBS
e = equilibrium conditions
G = gas phase
H = solid hydrate phase
I = solid ice phase

irG = irreducible gas
irA = irreducible aqueous phase
max = maximum
min = minimum
n = permeability reduction exponent – Table 2
P = production stream
R = rock, released
sw = swelling
v = volumetric

1 INTRODUCTION

Gas hydrates occur naturally offshore at shallow depths below the seafloor and onshore beneath the permafrost. Hydrates contain enormous quantities of methane gas, which if economically producible, can make a significant contribution to the future energy supply. Interest in gas hydrates has increased in recent years, with governments as well as several oil and gas producing companies initiating projects for drilling and testing of hydrate-bearing sediments (HBS). Given the sheer magnitude of the resources and the finite volume of conventional fossil fuel reserves, methane hydrates are emerging as a potential energy source for a growing number of nations, even if only a small portion of methane hydrates can be economically recovered (Moridis et al., 2009; 2011). Several production methods, including depressurization, thermal stimulation, and inhibitor injection, are being considered for extraction of gas from hydrate-bearing formations. However, the geomechanical response of HBS in general, and potential wellbore instability and casing deformation in particular, are serious concerns that need to be addressed and understood before commercial gas production from hydrate deposits can be developed (Moridis et al., 2009; 2011; Hancock et al., 2010).

Oceanic deposits that could be suitable for production often involve unconsolidated sediments of relatively high porosity, and are usually characterized by limited strength and high compressibility. The dissociation of the solid hydrates (a strong cementing agent) during gas production can degrade the structural strength of the HBS, which is further exacerbated by the evolution of an expanding gas zone, progressive transfer of loads from the hydrate to the sediments, and subsidence. The problem is greatest in the vicinity of the wellbore, where the largest changes are concentrated, and is further complicated by production-induced changes in

the reservoir pressure and temperature. Such pressure and temperature changes can significantly alter the local stress and strain fields, with direct consequences for wellbore stability, the flow and fluid properties of the system, the potential for co-production of solids, and (consequently) for continuing gas production. To assure a sustainable production in such a system, advanced well-engineering technology will be required, including adequate sand control and well assemblies that can withstand large reservoir compaction.

Carefully controlled drilling and well completion will be critical for gas production from an oceanic HBS. It will be important to carefully control the temperature and pressure of the drilling mud, keeping it sufficiently cool and at sufficiently high pressure to minimize hydrate dissociation during drilling and completion of production wells. Depending on site conditions, drilling and completion could be conducted overbalanced (at an internal well pressure higher than the formation fluid pressure) or slightly underbalanced (at an internal well pressure slightly lower than the formation fluid pressure). Overbalanced drilling at higher internal well pressure (mud pressure) may help to stabilize the wellbore during drilling and completion. Underbalanced drilling, using a mud pressure lower than the formation fluid pressure, may be desirable to avoid fine particles from the drilling mud entering and clogging the pore space in the formation adjacent to the well bore. Underbalanced drilling and completion could be especially beneficial for long-range horizontal wells completed with pre-slotted liner, because they are more difficult to clean up if the formation were to be damaged by invading mud solids. New completion technology, such as the use of expandable sand screens, could also be applied in gas production from oceanic HBS to reduce the annular space, thereby reducing annular flow, maximizing borehole volume, and stabilizing the borehole wall (Acock et al.,

2009). Some of these drilling and completion options are considered in the present modeling study, in particular with regard to the potential for well instability.

2 PROBLEM DESCRIPTION

The geologic system considered in this study is based on that of the Tigershark area (Smith et al. 2006) located in the Alaminos Canyon Block 818 of the Gulf of Mexico. This area has been the subject of previous studies to assess production potential (e.g., Moridis and Reagan, 2007a,b; Rutqvist and Moridis, 2009). Log data from an exploration well in about 2750 m (9000 ft) of water at the site indicated the presence of an 18.25 m (60 ft) thick sandy hydrate bearing sediment (HBS) (10,530 to 10,590 ft drilling depth) with a porosity ϕ of about 0.35 and Darcy-range intrinsic permeability. Preliminary calculations indicate that the hydrate saturation S_H is in the 0.6-0.8 range, and that the base of the gas hydrate stability zone at this location occurs at or slightly below the base of the HBS (Smith et al., 2006; Collett and Lee., 2006).

Gas production from this deposit was investigated by Moridis and Reagan (2007a,b) for production from a Class 3 deposit, i.e., composed of a single hydrate interval and bounded by confining (impermeable) layers, or a Class 2 deposit, i.e., with a zone of mobile water underlying the hydrate layer. In the case of a Class 3 deposit, a constant flowing bottom-hole well pressure production was employed, whereas in the case of a Class 2 deposit, constant-rate production was employed. A constant flowing bottom-hole pressure production method is recommended in Class 3 deposits, because of uncertainties over (a) the magnitude of the effective permeability of the original (undisturbed) HBS, and (b) the permeability evolution

over time (Moridis and Reagan, 2007b). These uncertainties preclude constant-rate production.

Rutqvist and Moridis (2009) investigated production performance and geomechanical responses during depressurization-induced gas production from the same hydrate deposit, but using a horizontal well. They found that the use of long-range horizontal production wells is an attractive option for producing from a Class 2 HBS. Moreover, they found that away from the immediate surroundings of the production well, dissociation, phase saturations and flow patterns are surprisingly uniform and have smooth gradients. This uniformity and smoothness has important implications for the study of HBS geomechanical behavior, because it results in a rather uniform stress distribution and subsidence over the entire length of the depressurized reservoir. However, the geomechanical analysis in Rutqvist and Moridis (2009) also indicated that depressurization-based gas production from oceanic hydrate deposits may significantly affect the geomechanical stability of HBS if structurally weak formations are involved.

In this study, we investigate the geomechanical performance with special emphasis on wellbore geomechanical issues for alternative cases of gas production:

- Case 1: Constant flowing bottom-hole pressure production from a Class 3 deposit using horizontal wells
- Case 2: Constant-rate production from a Class 2 deposit using vertical wells

We compare the geomechanical responses and the potential adverse geomechanical effects for the two different cases. The simulations are conducted at two model scales, because stress evolution near the wellbore critically depends on the reservoir scale-evolution of pressure,

temperature, while wellbore instability also critically depends on local wellbore design (including casing, liner, and perforation), We first conducted reservoir-scale model simulations of Case 1 and 2 to obtain quantitative estimates of the evolution of coupled hydraulic, thermodynamic and geomechanical evolution both in the reservoir and near the production wells. We then conducted wellbore-scale model simulations to calculate the detailed geomechanical evolution adjacent to the wellbore and the wellbore assembly. The wellbore-scale model simulation uses results from the reservoir-scale simulations for boundary and interior conditions, including the evolution of pressure, temperature, hydrate saturation, and stresses.

3 GEOMECHANICAL PROPERTIES OF THE HBS

The geomechanical properties of HBS were derived from laboratory experiments by Masui et al. (2005, 2008) and Miyazaki et al. (2010, 2011) on reconstituted hydrate-bearing Toyoura sand as well natural offshore samples from Nankai Trough, Japan. We use a Mohr-Coulomb elastoplastic constitutive mechanical model in which the parameters describing the mechanical properties are corrected for pore-filling solid content (hydrate and ice). Based on the experimental results of Masui et al. (2005, 2008) and Miyazaki et al. (2010, 2011), we assume that certain mechanical properties (bulk and shear moduli, and cohesion) increase linearly with hydrate saturation (Table 1). For example, from the data of Masui et al. (2005, 2008) we derived the cohesion values ranging from 0.5 MPa at 0% hydrate saturation to an extrapolated 2.0 MPa at 100% hydrate saturation; this results in a hydrate-dependent shear strength that matches the laboratory data quite well over relevant ranges of hydrate content (Figure 1). Additionally, according to the experimental results of Masui et al. (2005, 2008),

the friction angle is independent of the hydrate saturation and equal to 30°. A dilation angle of 10° is adopted in a non-associated elasto-plastic Mohr-Coulomb model. We assume that the dilation angle is independent of hydrate content, although the experimental results by Masui et al. (2005, 2008) indicate a slight increase in the dilation angle with hydrate content. The mechanical properties derived from Masui et al. (2005, 2008) and Miyazaki et al. (2010, 2011) were chosen because of the lack of published geomechanical data on hydrate bearing Gulf of Mexico sand, and because the data set of Masui et al. (2005, 2008) and Miyazaki et al. (2010, 2011) is (to the author's knowledge) the most complete and systematic geomechanical strength data set of HBS available to date. Moreover, the geomechanical properties (strength and compressibility) of the Toyoura sand is consistent with typical deep water Gulf of Mexico unconsolidated sand of relatively high porosity (Zoback, 2007).

4 THE NUMERICAL SIMULATION CODE

For the analysis of the geomechanical behavior of HBS, we applied a numerical model that integrates a commercial geomechanical code into a simulator describing the coupled processes of fluid flow, heat transport, and thermodynamic behavior in geologic media. The simulator couples the TOUGH+HYDRATE simulator (Moridis, 2003; Moridis et al. 2008), which describes the system hydraulic, thermal, and thermodynamic behavior in geological media containing gas hydrates, to the FLAC^{3D} (Itasca, 2009) geomechanical simulator (Figure 2). The coupled simulator is described in more detail in Rutqvist and Moridis (2009), and has been applied to investigate the geomechanical performance of both oceanic and permafrost related HBS (Rutqvist et al. 2009a,b). The TOUGH+HYDRATE code predicts the evolution of all the important thermophysical properties (e.g., pressure, temperature, phase saturation

distribution, salt concentration) in hydrate-bearing systems undergoing changes through any combination of mechanisms that can induce hydrate dissociation or formation, i.e., changes in pressure, temperature, and/or in the concentration of inhibitors (such as salts and alcohols). The FLAC^{3D} code has built-in constitutive mechanical models suitable for soil and rock, including various elastoplastic models for quasi-static yield and failure analysis, and viscoplastic models for time-dependent (creep) analysis, that could be used directly or modified for analyzing the geomechanical behavior of HBS.

In the resulting coupled simulator, the two constituent codes—TOUGH+HYDRATE and FLAC^{3D}—are linked through a coupled thermal-hydrological-mechanical (THM) model of the HBS. The THM model is consistent with the porous media model (one of the several available as options in TOUGH+HYDRATE) that describes media deformation as a result of geomechanical changes. In addition, there are numerous couplings—including changes in mechanical and hydrological properties—that are consequences of changes in effective stress and pore volume. The relationship between hydraulic and geomechanical properties is further complicated by couplings related to temperature changes, and the possible effects of inhibitors. (Salts are present in all oceanic hydrate deposits, and salts and alcohols are occasionally used to enhance hydrate dissociation).

Because this study is focused on the geomechanical behavior of the HBS, and the potential for wellbore instability and casing deformation, we limit our simulations to one-way coupled analyses. That is, we investigate the effects that changes in P, T, and S_H induce on the geomechanical behavior of HBS and wellbore stability (as described by all relevant

geomechanical parameters), but we do not account for the effect of the mechanically induced changes in hydraulic and wettability properties on the multiphase flow behavior. Such complete (two-way) coupling has been studied in (Kim et al., 2012a; 2012b) for modeling issues related to reservoir geomechanical behavior, including potential irreversible deformations within the reservoir and adjacent caprock. In such two-way coupled analysis, additional failure can be induced as a result of poro-elastic stress changes in the low permeability caprock, as well as within reservoir, far away from the production well.

5 MODEL SETUP

As mentioned above in the introduction, we divide this analysis into reservoir-scale and wellbore-scale model simulations. The reservoir-scale model simulations are conducted on reservoir-scale model domains, which are different for Case 1 and Case 2 (Figure 3). Thereafter, wellbore-scale simulations are conducted on a wellbore-scale model domain having different initial and boundary conditions derived from the results of the previous reservoir-scale model simulation (Figure 4).

5.1 Case 1 reservoir-scale model domain

The model setup of the reservoir-scale model for production from a Class 3 HBS using horizontal wells is shown in Figure 3a. The case involves a system of parallel horizontal wells, with a well spacing of 1,000 m (3,281 ft). Within the HBS, the horizontal well is located 1 m below an overlying, low-permeability shale layer. Hydrate is depressurized by applying a constant flowing bottom-hole pressure Pw = 2.8 MPa (406 psi). The geometry of the simulated domain represents a unit length (= 1 m) of the horizontal well and extends laterally 500 m (1,640 ft). Because of symmetry, there is no flow of fluids and heat through the lateral boundaries (vertical sides) of the domain. For the same reason, we impose a

restriction of zero displacement normal to these boundary surfaces. The top boundary, representing the seafloor, is kept at constant temperature, T and pressure, P, but is allowed to move. The bottom boundary (placed at a depth of 30 m below the hydrate layer) has a fixed P and T, and a restriction of zero displacement along the z-axis, i.e., normal to the boundary.

5.2 Case 2 reservoir-scale model domain

The model setup of the reservoir-scale model for production from a Class 2 HBS using vertical wells (Figure 3b) is equivalent to that of Moridis and Reagan (2007a). The system involves vertical wells with well spacing of about 800 m (2580 ft). The well design and production method are also similar to that of Moridis and Reagan (2007a), involving a 6 m long production (perforated) interval with a radius 0.1 m extending from the HBS/WZ (water zone) contact 2 m up into the HBS and 4 m down into the WZ. The outer wellbore surface is initially heated at a power of 300 W over its vertical extent across the HBS. This heating causes thermal dissociation of the hydrate and leads to the creation of a dissociated cylindrical high permeability zone around the production well. Moreover, the well design considered in this case allows for injection of warm water from the well into the HBS at a location just below the upper confining shale layer. The top boundary, representing the seafloor, is kept at constant T and P, but is allowed to move. The bottom boundary (placed at a depth of 30 m below the WZ) has a fixed P and T, and a restriction of zero-displacement along the z-axis, i.e., normal to the boundary. The initial mass production from the well is 18.5 kg/s.

5.3 Wellbore-scale model domain

The wellbore-scale simulations were conducted using 2-D plane-strain or plane-stress models (Figure 4). For modeling a horizontal well, a 2-D plane strain model was used to represent a vertical cross section through the well, whereas for a vertical well, a 2-D plane stress model

was used to represent a horizontal plane. In both the plane strain and plane stress models, the initial tri-axial stress field is given as shown in Figure 4 left and middle. The models extend about 0.5 m from the well into the formation, beyond any significant stress concentrations around the wellbore. Time-dependent boundary and interior conditions for the wellbore scale simulation were extracted from the reservoir-scale simulation results for both Case 1 (horizontal well) and Case 2 (vertical well). The well casing or liner is simulated using special mechanical so-called liner elements available in FLAC^{3D}. The liner elements can model resistance to both membrane and bending loads. In addition, the liner element models a shear-directed (in the tangent plane to the liner surface) frictional interaction. Thus, with this approach, we can capture the frictional sliding along the interface between the casing and the formation. We used the liner element for a generic representation of alternative well designs, such as cased and cemented vertical well or horizontal well with a liner. As will be described in more detail below, we also considered different drilling and well completion sequences, such as overbalanced drilling (at a mud pressure higher than the formation fluid pressure) and the effects of an annular gap between the well casing (or liner) and the formation.

5.4 Initial conditions and material properties

The initial conditions, and the most relevant multiphase flow and heat transport properties, are provided in Table 2 for both Case 1 and Case 2. The initial temperature distribution was computed from the known temperature at the seafloor mud line (reported as 5°C) and the corresponding geothermal gradient. The pressures in the subsurface profile were assumed to follow a hydrostatic distribution. Initial pressures were computed using the water depth at the site of 2800 m (9186 ft), and a pressure-adjusted saline water density typical of ocean water (1003 kg/m^3 at atmospheric pressure). We assumed an isotropic initial stress that increases

with depth below the seafloor, for a bulk density of 2600 kg/m^3. The isotropic stress assumption means that the initial maximum and minimum horizontal stresses are equal to the initial vertical stress, and they are all calculated from the weight of the overburden. At the HBS, 470 m below the seafloor, the load from the water column and 470 m of sediments results in a high initial stress of about 40 MPa (5800 psi), whereas the initial effective stress (total stress less fluid pressure) is only about 7.5 MPa (1090 psi). In Case 1, we also considered slightly permeable (1×10^{-19} m^2 or 100 nanoDarcy), bounding shale layers to investigate the potential effects of pressure depletion that the shale layers might have on geomechanical performance.

6 CASE 1 RESERVOIR-SCALE SIMULATION RESULTS (HORIZONTAL WELL)

This simulation was conducted with a constant bottom hole pressure Pw = 2.8 MPa (406 psi) at the well for 2 years. A 2-year simulation was sufficient for our wellbore stability analysis because thermo-dynamic and geomechanical changes occur within a few days near the well and reach a pseudo-steady state within a few months in the reservoir.

6.1 Case 1 Production Rates

CH_4 gas and water production rates for Case 1 are shown in Figure 5, calculated for an assumed 500 m long horizontal production well. As shown in Figure 5a, the calculated gas production is initially high, above 32 ST m^3/s (cubic meters per second at standard conditions), corresponding about 100 MMscfd (million standard cubic feet per day). The initial high production results from a steep pressure gradient after an instantaneous reduction of well pressure to 2.7 MPa (406 psi). In the field, the constant bottom-hole pressure could not be applied instantaneous, but might be established after some time, e.g. one after 1 month of

production. In the model simulation, the production then drops rapidly to less than 3 STm^3/s (9 MMscfd) after a year, and finally declines to about 1.1 ST m3/s (~3.4 MMscfd) after 2 years of production. Water production also starts out high at about 0.09 m^3/s, corresponding to about 48,900 bwpd (barrels of water per day) at a water-gas ratio of 489 bbls/MMscf (Figure 5b). The water production then decreases with time, and after 2 years it is about 5.5×10^{-4} m^3/s (299 bwpd) at a water-gas ratio of about 88 bbls/MMscf. Such high initial production and water rates will require special well completion requirements as discussed by Hancock et al. (2010). For example, some large well diameter and tubing, and some form of artificial lift will be required to maintain a constant flowing bottom-hole pressure as low as 2.7 MPa (406 psi).

6.2 Case 1 reservoir-scale thermodynamic evolution

Figure 6 shows the temporal evolution of pressure, temperature, and hydrate saturation at monitoring points P1 and P2 located respectively, 0.5 and 10 m horizontal distance away from the production well, whereas Figure 7 shows the spatial distributions after 6 months. At the well (P1 in Figure 6), the pressure and temperature drop so rapidly that the hydrate dissociates almost instantaneously (Figure 6c). The pressure depletion is very efficient along the reservoir, with a pressure drop from an initial average reservoir pressure (averaged over the entire reservoir) of 32.5 MPa (4,786 psi), to about 3 MPa (435 psi), as dictated by the constant flowing bottom-hole pressure P_w = 2.7 MPa (406 psi) at the well (Figure 6a and 7a). The cooling of the HBS (a direct consequence of the hydrate dissociation) results in a temperature drop from 21°C to about 2°C (Figure 6b and 7b). Later the temperature partially recovers at P1 and P2, because of heat supplied from the upper shale layer. At 6 months, the dissociation front has receded only a few meters from the well at the mid level of the HBS, but several

hundred meters along the top and bottom boundaries of the HBS (Figure 7c). Gas from the hydrate dissociation accumulates under the low-permeability shale (Figure 7d) and then flows towards the production well, where it is produced.

6.3 Case 1 reservoir-scale stress and strain evolution

Figure 8 presents the evolution of total and effective principal stresses at P1 and P2. At P1 (x = 0.5 m), the stress field first reacts to the local pressure changes near the wellbore (compare pressure evolution in Figure 6a with stress evolutions in Figures 8a and b). At x = 10 m, the stress evolution is somewhat delayed similarly to the delayed pressure evolution at x = 10 m. Overall, the production (and the corresponding depressurization) tends to increase the reservoir shear stress—which is proportional to the difference between the maximum and minimum principal stresses. Shear stress increases because depressurization causes poroelastic stressing in the mechanically confined horizontal direction, whereas the vertical stress remains roughly constant, equal to the weight of overburden sediments.

Figure 8c presents the path of the maximum and minimum principal effective stresses. The principal stresses at x = 0.5 and 10 m quickly merge and follow the same path of increasing effective stress. After 1 day, the stress path changes slowly toward the Mohr-Coulomb failure surface. However, the Mohr-Coulomb failure surface is never reached within 2 years of production, and the stress state has reached a pseudo steady state.

Figures 9a and b present calculated volumetric strain after 6 months and 2 years, respectively, and Figure 9c presents vertical seafloor subsidence over the 2 years of simulated gas

production. The volumetric strain in Figures 9a, b is essentially vertical strain, because the vertical strain is much larger than the horizontal when the system is mechanically confined laterally. Subsidence takes place gradually as a function of time, despite reservoir pressure decreasing very rapidly. (Compare relative slow subsidence in Figure 9c to the very rapid pressure decline in Figure 6a.) However, the total subsidence not only depends on vertical compaction of the HBS, it also depends on vertical compaction of the adjacent shale layers. Initially, the subsidence is relatively rapid as a result of the rapid pressure decline and compaction of the HBS. At 2 years, the HBS compaction strain amounts to about 3.5%, resulting in about 0.8 m of vertical compaction. The remaining compaction leading to up to 4.5 m of seafloor subsidence is caused by the vertical compaction of the adjacent shale layers. Note that the adjacent shale layers are much thicker than the HBS, and pressure depletion of the shale layers can thereby substantially contribute to the total subsidence. Moreover, the maximum vertical compaction strain of 13% takes place within the shale layers, near their interface with the HBS (Figure 9b).

7 CASE 2 RESERVOIR-SCALE SIMULATION RESULTS (VERTICAL WELL)

The simulation for Case 2 was conducted for 4 years of gas production, starting with a constant-mass production rate of 18.5 kg/s under simultaneous electric heating of the well casing (at a power of 300 W). In the case of constant-rate production, we would not obtain the instantaneous pressure and temperature drop that was observed in Case 1, but rather a more gradual response to production.

7.1 Case 2 Production Rates

The initial mass production of 18.5 kg/s is mostly water mass, corresponding to about 0.0183 ST m^3/s of water, while gas is produced at a rate of about 0.18 ST m^3/s (Figure 10). The initial gas production is mainly a result of dissolved gas exsolution from the pore water and stays less than 0.2 STm^3/s (0.6 MMscfd) for more than 120 days (4 months). After about 120 days, the gas production increases rapidly, up to 3.5 ST m^3/s (10.6 MMscfd) at 240 days (about 8 months), because of vigorous gas production by hydrate dissociation. At 240 days, as a results of Joule-Thomson cooling, secondary hydrates form near the perforation of the well, blocking gas and water flow, causing cavitation (rapid pressure drop at the well), and choking production. In the model simulation, the well was remediated by temporarily shutting down production and injecting warm water. The water was injected around the well just below the upper confining shale layer, at rate of 0.001 kg/s (543 bwpd) and at a temperature of 60°C. The special well design for this kind of warm water injection is described in Moridis and Reagan (2007a). After continued production under continuous warm-water injection, a second cavitation occurred after about 315 days. Again, the well was shut down to let the heat from the injected warm water dissociate secondary hydrates. The production was then resumed, under continuous warm water injection, but at a reduced rate to avoid additional cavitations. Figure 10a shows that the CH_4 gas production peaks at about 5 STm^3/s (15 MMscfd) at the second cavitation, and thereafter gradually declines to less than 2 STm^3/s (6 MMscfd) for most of the 4 year production period. The water production is initially very high and remains quite stable during the first year at 0.0183 ST m^3/s (about 10,000 bwpd), with a water-gas ratio of 20,000 bbls/MMscf. Then, the water production gradually declines to below 0.01 ST m^3/s (about 5,400 bwpd), with a water-gas ratio of 400 bbls/MMscf during the last few years of production. Again, the special well design requirements for these production parameters

and conditions are discussed in Hancock et al. (2010), including artificial lift and large well completions.

7.2 Case 2 reservoir-scale thermodynamic evolution

Figure 11 shows the temporal evolution of pressure, temperature, and hydrate saturation at P1 and P2, whereas Figure 12 shows the spatial distribution of key variables after 6 months of production. Figure 11c shows that hydrate dissociates near the well (x = 0.5 in Figure 11c) within one day as a result of the simulated electric heating of the well casing. Figure 12 shows that after 6 months the high temperature around the well (Figure 12b) has led to the creation of a cylindrical dissociation interface around the well (Figure 12c), which is connected with the production interval and thereby enhances initial gas production. Once the hydrates start dissociating, the gas zone develops both at the top and bottom of the hydrate layer (Figure 12d) due to heat flow from the top shale and bottom shale layers. During cavitations 1 and 2, the temperature near the production perforation increases temporarily up to 50°C (Figure 11b). These temperature increases occur when production is shut down and warm water injected from above can migrate down to the perforation and dissociate any secondary hydrates. This secondary hydrate dissociation consumes heat, and in turn, causes a rapid cooling. As a result, strong temperature and pressure rises occur near the perforation, especially associated with cavitation 2. Under continued production at lower rates, and after 4 years, the pressure and temperature have declined to about 5 MPa and 7°C, respectively (Figure 11b).

7.3 Case 2 reservoir-scale stress and strain evolution

In general, the responses for total and effective stresses (Figures 13a and b) follow the reservoir fluid-pressure responses (Figure 13a). The stress fields at P1 and P2 differ somewhat

because of the existence of a hydraulic gradient around the perforated interval. During production, the total principal stresses are reduced near the wellbore, leading to a reduced surface load on the wellbore casing. At the instances of cavitation, there are some fluctuations in the stress field, which can be directly related to the fluctuations in fluid pressure seen in Figures 13a and b. Temperature fluctuations could also impact the stress evolution; one can estimate the maximum thermal stress from $\Delta\sigma_T = 3 \times K \times \Delta T \times \alpha_T$ (assuming a fully constrained sediment) where K is the drained bulk modulus, ΔT is temperature change, and α_T is the coefficient of linear thermal expansion. Assuming temperature change ΔT = 40°C, Young's modulus K = 95 MPa (Table 1 for hydrate free sand), and thermal expansion coefficient, α_T = 1×10^{-5} $°C^{-1}$, one arrive at a maximum thermal stress of about 0.11 MPa. This shows that in this case thermal stress is negligible compared to stress changes induced by fluid pressure changes. At both P1 and P2, the stress eventually reaches the Mohr-Coulomb failure surface (Figure 13c). Near the perforated interval at P1 (r = 0.5 m), the stress field approaches the failure surface after 2 years of production, and then follows the failure surface until 4 years have elapsed. The strong fluctuations in the well pressure and temperature during the cavitation did induce some damage to the formation adjacent to the well (inside 0.5 m), which then contributed to an irreversible reduction in minimum stress seen in Figure 13c.

Vertical subsidence also follows the pressure decline in the HBS and underlying water zone, and amounts to about 2.5 m after 4 years of production (Figure 14c). The total subsidence is mostly a result of vertical compaction of sediments within the hydrate free (and relatively soft) zone of mobile water (Figures 14a, b). In this zone, the vertical strain after 4 years is about 13%, whereas the strain in the HBS is limited to about 4% (Figure 14b). It is limited to

4% in the HBS because the hydrate dissociation front recedes slowly with time, and thus more compaction is to be expected in the HBS once it is completely dissociated.

8 WELLBORE-SCALE SIMULATION RESULTS FOR CASE 1 (HORIZONTAL WELL) AND CASE 2 (VERTICAL WELL)

We conducted a detailed analysis of mechanical interactions between the well assembly and the formation using the wellbore-scale model domain shown in Figure 4. As mentioned, the boundary and interior conditions for this wellbore-scale simulation were extracted from the reservoir-scale simulation results for both Case 1 (horizontal well) and Case 2 (vertical well). In the case of the horizontal well, we use the evolution of fluid pressure, temperature, and hydrate saturation from Figure 6 (at x = 0.5 m), as well as total stresses such as those shown in Figure 8a. In the case of a vertical well, we use evolution of pressure, temperature, and hydrate saturation shown in Figure 11, as well as total stress, such as those shown in Figure 13a.

We mentioned above the necessity of sand-control technology when producing gas from an HBS. According to Hancock et al. (2010), options for sand-control technologies associated with production from HBS include gravel packs, screens, or liners. In vertical wells, sand control can be accomplished using open- or cased-hole technologies, which can include wire-wrapped or premium mesh type screens, with gravel placed using cased or open hole circulation or frac-pack techniques. Horizontal wells will typically use wire-wrapped screens without gravel, based on cost, concerns over effective gravel placement over long horizontal lengths, and hole clean-out and plugging concerns using premium screens (Hancock et al.,

2010). Moreover, in unconsolidated HBS, well instability could be expected, and therefore the screen may be run inside a pre-perforated liner (Garrouch et al. 2004). One important feature to consider in our geomechanical wellbore model is the potential for an annular gap between casing (or liner) and the formation, as well as drilling mud pressure and temperature. Here we assume that the drilling mud temperature is carefully controlled and equal to the formation temperature during drilling and completion, thus keeping it sufficiently cool to minimize unwanted hydrate dissociation. We then consider three cases of drilling and well completions:

1) **Balanced drilling and completion with 1-1/2 inch annular gap:** We assume a drilling mud pressure in balance with formation fluid pressure during drilling and then installation of well casing or liner with an annular gap of 1.5 inch (3.8 cm) to the formation. For example, this could represent driving a 5-1/2 inch liner in an 8-1/2 inch horizontal wellbore.

2) **Balanced drilling and completion with no annular gap:** We assume a drilling mud pressure in balance with formation pressure and the use of expandable screens or other completion methods (such as casing and cement or open hole gravel pack) that would eliminate the annular gap. This case would still involve some contraction of the wellbore during drilling, since the internal wellbore pressure (drilling mud pressure) is less than the in situ stress magnitude.

3) **Overbalanced drilling and completion with no annular gap:** We assume drilling with drilling mud pressure significantly higher than the formation pressure (overbalanced) and equal to the isotropic is situ stress at the site. Moreover, we assume installation of an expandable screen or other completion methods that would eliminate the annular gap.

Figures 15 and 16 summarize the results of the analysis for the three cases of drilling and well completions, for horizontal and vertical well cases, respectively. In general, some plastic yielding occurs around the wellbore in all cases, but the extent of the yield zone can be reduced when using overbalanced drilling and well completion that minimizes the annular gap.

The simulations showed that using drilling mud pressure in balance with the formation fluid pressure, the wellbore contracts radially about 2 cm during simulated drilling, and a small yield zone forms around the wellbore. This can be observed in Figures 15 and 16 for contours after 1 day in the two left-most columns, in which balanced drilling and completion is assumed. Also note that after 1 day, the hydrate has already been dissociated around the wellbore for both Case 1 and Case 2. This means that even if the hydrate around the wellbore had dissociated already during drilling, the results of yielding at 1 day will be equivalent as shown in Figures 15 and 16. During production, the yield zone may expand further from the wellbore because of reduced well pressure, hydrate dissociation, and increased shear stresses around the wellbore. If the drilling fluid were to be slightly underbalanced, the initial wellbore contraction would be larger than 2 cm and additional yielding would be induced.

The case with balanced drilling and well completion that leaves a 1.5 inch (3.8 cm) annular gap resulted in the most extensive yield zone around the wellbore. In this case, the wellbore first contracted 2 cm during the simulated drilling, and then during production it contracted further to fill in the 1.5 inch (3.8 cm) annular gap.

In the case of overbalanced drilling, mud pressure was assumed to be about 7 MPa (about 1,000 psi) higher than the formation fluid pressure. That is, mud pressure was set to 32.5 + 7 = 39.5 MPa. Such mud pressure may be considered an upper limit, as any increase over 7 MPa could result in fracturing of the formation around the wellbore. However, the overbalanced drilling and completion supports the wellbore until the casing or expandable screen is set, which is beneficial from a wellbore stability perspective. For example, in the case of a vertical wellbore, the initiation of yielding around the wellbore did not occur until after 1 year of production.

The resulting evolution of the yield zone during production is different for vertical and horizontal wells. In both cases, the evolution is driven by the reservoir pressure decline and associated increases in vertical effective stress and shear stress. In the case of a horizontal well, the increased vertical effective stress and associated compaction acting on and around the relatively stiff well casing (or liner) results in some additional yielding on the top and sides of the well. However, the yield zone is quite limited in extent, and most of the yielding occurs during drilling and completion when the wellbore is allowed to contract radially. In the case of a vertical well, the yield zone expands radially over the 4-year production period, along with the pressure decline. The extent and magnitude of the yield increase somewhat in the case of a 1.5 inch (3.8 cm) annular gap. In fact, simulation shows that if no casing (or liner) is used, the wellbore would be unsupported and would collapse completely during production.

From the stress paths shown in Figures 15 and 16 we may also estimate the maximum stress acting against the surface of the well casing (or liner). For a horizontal well, we see that the maximum principal effective stress increases substantially to about 55 MPa (8,000 psi) at the top (and bottom) of the casing (or liner), whereas at the side of the well, the stress decreases with production. For a vertical well, the stress normal to the well casing (or liner) also decreases with production. The maximum stress of 55 MPa occurring on top of the horizontal well is the maximum stress that the formation can sustain under yielding.

9 DISCUSSION OF POTENTIAL PRODUCTION-INDUCED DAMAGE TO WELL ASSEMBLY

The greatest threats to the well assembly are excessive compaction and sand production. Excessive sand production would result in the creation of a cavern, leaving parts of the downhole well assembly unsupported. Again, adequate sand control is essential. A substantial vertical subsidence, on the other hand, is unavoidable, since efficient gas production from HBS calls for a substantial pressure drawdown. Our analysis indicates that vertical compaction strains could locally exceed 10%, resulting in several meters of compaction and seafloor subsidence. Reservoir subsidence is a common problem in many fields, not just in gas production from HBS. Typically, reservoir compaction greater than approximately 5% appears to be a consistent indicator for potential casing failures (Moridis et al., 2011). Thus, it appears that the vertical strains exceeding 10% calculated in this study might be prone to tensile failures in the casing above the reservoir, and buckling failure within the reservoir.

In this case, the HBS consist of soft unconsolidated sediments, so it is not clear if buckling within the formation could occur. However, if the well is cemented through the overlying shale layer, the vertical compaction could pull down the well casing, causing tensile failure a few hundred feet above the production interval. As mentioned, such tensile failures may be prevented through the use of slip joints or length expandable casing joints, whereas casing failures due to column buckling in the reservoir interval can be prevented by selecting heavy wall casings and by employing good cementing and solids-control practices (Hancock et al. 2010). Finally, in this simulation study, the properties within each layer are assumed to be homogenous and initial stress field was assumed isotropic, whereas in the field sediments spatial heterogeneities and intersecting faults and anisotropic stress field can have a substantial impact on the geomechanical behavior, which could also impact the well stability for both vertical and horizontal wells. For example, in the case of horizontal production wells heterogeneous compaction and subsidence due to sediment heterogeneities could lead to bending of the well pipes and if intersected by a fault could result in significant shear force across the well.

10 SUMMARY AND CONCLUSIONS

In this study we investigated coupled multiphase flow, thermal, thermodynamic and geomechanical behavior of oceanic HBS, during depressurization-induced gas production in general, and wellbore stability and potential casing deformation in particular. We investigated the geomechanical changes and wellbore stability for two alternative cases of production, using horizontal wells in a Class 3 deposit and vertical wells in a Class 2 deposit. We compared the geomechanical responses and the potential adverse geomechanical effects for

the two different cases. Based on the results of this study, the following conclusions can be drawn:

(1) Geomechanical responses during depressurization-based gas production from oceanic hydrate deposits are driven by the reservoir-wide pressure decline, ΔP, which is in turn controlled by the depressurization-induced pressure decline near the wellbore. Because pressure change quickly propagates within the reservoir, the reservoir-wide geomechanical response can occur within a few days of well pressure drawdown. In the case of a constant flowing bottom-hole pressure production from a horizontal well, most geomechanical changes occur within a few days. For a constant rate production from a vertical wellbore, the pressure decline and geomechanical changes occur synchronously and gradually with time.

(2) Vertical compaction and increased shear stresses are likely to cause local yielding of the formation around the well casing (or liners), but the extent of the yield zone can be reduced if using overbalanced drilling and well completion that minimizes any annular gap between the casing (or liner) and the formation. We found the most extensive yield zone for a vertical well, in particular around the perforated production interval where the pressure gradient is the highest. In practice, such yielding and shearing of the sediments leads to breaking of bonds between sand grains, which in turn could result in sand production if not prevented with appropriate sand control technology.

(3) The depressurization of the reservoir causes vertical subsidence that depends on the magnitude of pressure decline, ΔP, as well as the elastoplastic properties of the host sediment. Our analysis shows that the vertical compaction of the reservoir can

The simulations in this study were conducted using a Mohr-Coulomb shear failure criterion, whereas the potential for compaction yield as a result of increasing mean stress was not considered. Compaction yield could have an impact on the calculated extent of the failure zone around the well, especially in the case of a horizontal well. Compaction yield can be analyzed using a cap model (e.g. Rutqvist et al. 2011; Sultan and Garziglia, 2011). Moreover, in case of rapid compaction, a two-way pore-volume coupling might result in additional transient pore-pressure effects (e.g. Kim et al., 2012a). Nevertheless, our study clearly shows that the issue of geomechanical stability, including wellbore and casing stability needs to be carefully assessed at any field site involving HBS. Coupled geomechanical analysis of this type can be used for designing production strategies for optimized production, and at the same time for avoiding damaging geomechanical changes.

ACKNOWLEDGMENTS

This work was supported by the Assistant Secretary for Fossil Energy, Office of Natural Gas and Petroleum Technology, through the National Energy Technology Laboratory, under the U.S. Department of Energy, Contract No. DE-AC02-05CH11231. The authors extend their thanks and appreciation to Dan Hawkes, Matthew Reagan and John Apps for their careful review and their helpful comments.

REFERENCES

Acock, A., ORourke, T., Shirmboh, D., Alexander, J., Anderson, G., Kaneko, T., Venkitaraman, A., Lopez-de-Cardenas, J., Nishi, M., Numazawa, M., Yoshioka, K., Roy, A., Wilson, A., Twynam, A., 2004. Practical Approaches to Sand Management. In: Oilfield Review, Spring 2004.

Collett, T.S., Lee, M.W., 2006. Well Log Analysis: Tiger Shark AC 818 No. 1, U.S. Geological Survey, internal memo.

Hancock, S., Moridis, G.S., Wilson, S., Robertson, A., 2010. Well design requirements for deepwater and arctic onshore gas hydrate production wells. OTC-21015. Paper presentation at the 2010 Offshore Technology Conference held in Houston, Texas, U.S.A., 3–6 May, 2010.

Itasca, 2009. FLAC3D, Fast Lagrangian Analysis of Continua in 3 Dimensions, Version 4.0. Minneapolis, Minnesota, Itasca Consulting Group, 438pp.

Kim, J., Moridis, G.J., Yang, D., Rutqvist, J., 2012a. Numerical studies on two-way coupled fluid flow and geomechanics in hydrate deposits. SPE Journal (In Press).

Kim, J., Moridis, G.J., Rutqvist, J., 2012b. Coupled flow and geomechanical analysis for gas production in the Prudhoe Bay Unit L-106 Well Unit C gas hydrate deposit in Alaska. Journal of Petroleum Science and Engineering, (In Press).

Masui, A., Haneda, H., Ogata, Y., Aoki, K., 2005. The effect of saturation degree of methane hydrate on the shear strength of synthetic methane hydrate sediments. Proceedings of the 5th International Conference on Gas Hydrates, Trondheim, Norway, 657–663.

Masui, A., Miyazaki, K., Haneda, H., Ogata, Y., Aoki, K., 2008. Mechanical characteristics of natural and artificial gas hydrate bearing sediments. Proceedings of the 6th International Conference on Gas Hydrates (ICGH 2008), Vancouver, British Columbia, Canada, July 6–10, 2008.

Moridis, G.J., 2003. Numerical Studies of Gas Production From Methane Hydrates, SPE Journal. 32(8), 359-370.

Moridis, G.J., Reagan, M.T., 2007a. Gas Production From Oceanic Class 2 Hydrate Accumulations", OTC 18866, 2007 Offshore Technology Conference, Houston, Texas, U.S.A., 30 April–3 May, 2007.

Moridis, G.J., Reagan, M.T., 2007b. Strategies for Gas Production From Oceanic Class 3 Hydrate Accumulations," OTC 18865, 2007 Offshore Technology Conference, Houston, Texas, U.S.A., 30 April–3 May, 2007b.

Moridis, G.J., Kowalsky, M., Pruess, K., 2008. TOUGH+HYDRATE v1.0 User's Manual. LBNL-161E, Lawrence Berkeley National Laborotory, Berkeley, CA.

Moridis, G.J., Collett, T.S., Boswell, R., Kurihara, M., Reagan, M.T., Koh, C., Sloan, E.D., 2000. Challenges, Toward Production from Gas Hydrates: Current Status, Assessment of Resources, and Simulation-Based Evaluation of Technology and Potential. SPE Res Eval & Eng. 12(5), 745-771. SPE-114163-PA. doi: 10.2118/114163-PA.

Moridis, G.J., Collett, T.S., Pooladi-Darvish, M., Santamarina, C., Boswell, R., Kneafsey, T.J., Rutqvist, J., Kowalsky, M.B., Reagan, M.T., Sloan, E.D., Sum, A., Koh, C., 2011. Challenges, Uncertainties, and Issues Facing Gas Production From Gas-Hydrate

Deposits. Society of Petroleum Engineers, SPE Res Eval & Eng. 14 (1), 76-112. SPE-131792-PA. doi: 10.2118/131792-PA.

Miyazaki, K., Masui, A., Tenma, N., Ogata, Y., Aoki, K., Yamaguchi, T., Sakamoto, Y., 2010. Study on Mechanical Behavior for Methane Hydrate Sediment Based on Constant Strain-Rate Test and Unloading-Reloading Test Under Triaxial Compression, Int. J. Offshore Polar Eng. 20, 61-67.

Miyazaki, K., Masui, A., Sakamoto, Y., Aoki, K., Tenma, N., Yamaguchi, T., 2011. Triaxial compressive properties of artificial methane-hydrate-bearing sediment. Journal of Geophysical Research. 116, B06102.

Rutqvist, J., Moridis, G.J., Kim, J., 2011. A numerical study of gas production from collapsing oceanic hydrate-bearing sediments. Proceedings of the 7th International Conference on Gas Hydrates (ICGH 2011), Edinburgh, Scotland, United Kingdom, July 17-21.

Rutqvist, J., Moridis, G.J., 2009. Numerical Studies on the Geomechanical Stability of Hydrate-Bearing Sediments. Society of Petroleum Engineers, SPE Journal. 14, 267-282. SPE-126129.

Rutqvist, J., Moridis, G.J., Grover, T., Collett, T., 2009. Geomechanical response of permafrost-associated hydrate deposits to depressurization-induced gas production. Journal of Petroleum Science and Engineering. 67, 1–12.

Smith, S., Boswell, R., Collett, T., Lee, M., Jones, E., 2006. Alaminos Canyon Block 818: A Documented Example of Gas Hydrate Saturated Sand in the Gulf of Mexico. Fire In The Ice: NETL Methane Hydrates R&D Program Newsletter, 12 (Fall 2006).

Sultan, N., Garziglia, S., 2011. Geomechanical constitutive modeling of gas-hydrate-bearing sediments. Proceedings of the 7th International Conference on Gas Hydrates (ICGH 2011), Edinburgh, Scotland, United Kingdom, July 17-21.

van Genuchten, M.T., 1980. A Closed-Form Equation for Predicting the Hydraulic Conductivity of Unsaturated Soils", Soil Sci. Soc. 44, 892.

Zoback, M., 2007. Reservoir Geomechanics. Cambridge University Press, Cambridge, UK.

Tables

Table 1 – Input geomechanical properties

Parameter	**Value**
Cohesion C_m (MPa)	0.5 at $S_H = 0$ 2.0 at S $S_H = 1$
Friction angle (°)	30
Dilation angle (°)	10
Bulk modulus K (MPa)	95 at $S_H = 0$ 670 at $S_H = 1$
Shear modulus G (MPa)	87 at $S_H = 0$ 612 at $S_H = 1$
Coefficient of linear thermal expansion α_T ($°C^{-1}$)	$1x10^{-5}$
Biot's coefficient α_B (-)	1

Table 2 – HBS Thermodynamic Properties (Moridis and Reagan, 2007a, b)

Parameter	Value
Initial pressure P_B (at base of HBS)	3.3×10^7 Pa
Initial temperature T_B (at base of HBS)	294.15 K
Gas composition	100% CH_4
Water salinity (mass fraction)	0.03
Initial saturations in the HBS	$S_H = 0.7$, $S_A = 0.3$
Intrinsic permeability $k_x=k_z$ (HBS and water zone)	7.5×10^{-13} m^2 (= 0.75 D)
Intrinsic permeability $k_x=k_z$ (overburden & underburden)	1.0×10^{-19} m^2 (= 0.1 μD) in Case 1 0 m^2 (= 0 D) in Case 2
Grain density ρ_R (all formations)	2750 kg/m^3
Constant flowing bottom-hole pressure at the well P_w	2.7×10^6 Pa
Dry thermal conductivity $k_{\Theta RD}$ (all formations)	0.5 W/m/K
Wet thermal conductivity $k_{\Theta RW}$ (all formations)	3.1 W/m/K
Composite thermal conductivity model (Moridis et al., 2008)	$k_{\Theta C} = k_{\Theta RD} + (S_A^{1/2}+S_H^{1/2}) (k_{\Theta RW} - k_{\Theta RD}) + \phi S_I k_{\Theta I}$
Capillary pressure model (van-Genuchten, 1980; Moridis et al., 2008)	$P_{cap} = -P_0 \left[(S^*)^{-1/\lambda} - 1 \right]^{\lambda}$ $S^* = \frac{(S_A - S_{irA})}{(S_{mxA} - S_{irA})}$
S_{mxA}	1
λ	0.45
P_0	10^5 Pa
Relative permeability Model (Moridis et al., 2008)	$k_{rA} = (S_A^*)^n$ $k_{rG} = (S_G^*)^n$ $S_A^*=(S_A-S_{irA})/(1-S_{irA})$ $S_G^*=(S_G-S_{irG})/(1-S_{irA})$ OPM model
n (from Moridis and Reagan 2007a)	3.572
S_{irG}	0.02
S_{irA}	0.25

Figures

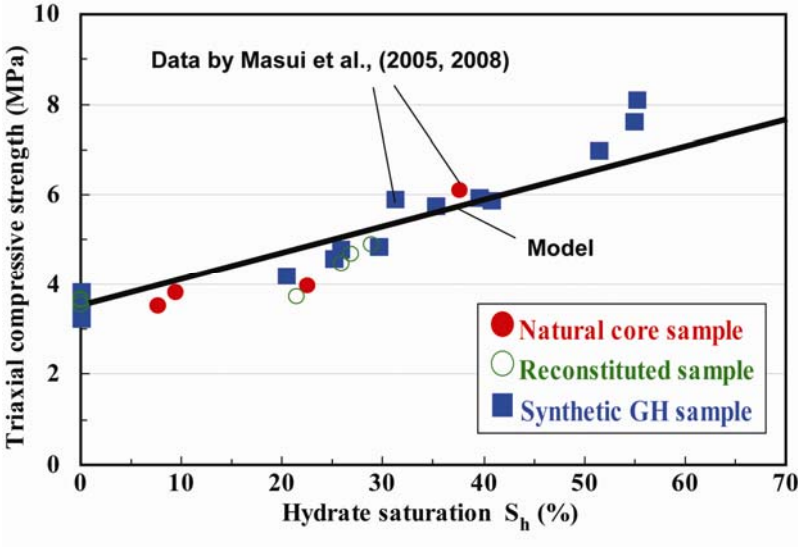

Figure 1 – Laboratory data of triaxial compressive strength from Masui et al. (2005, 2008) on artificial and natural samples of hydrate-bearing sand and linear dependency of hydrate saturation on strength adopted in this study.

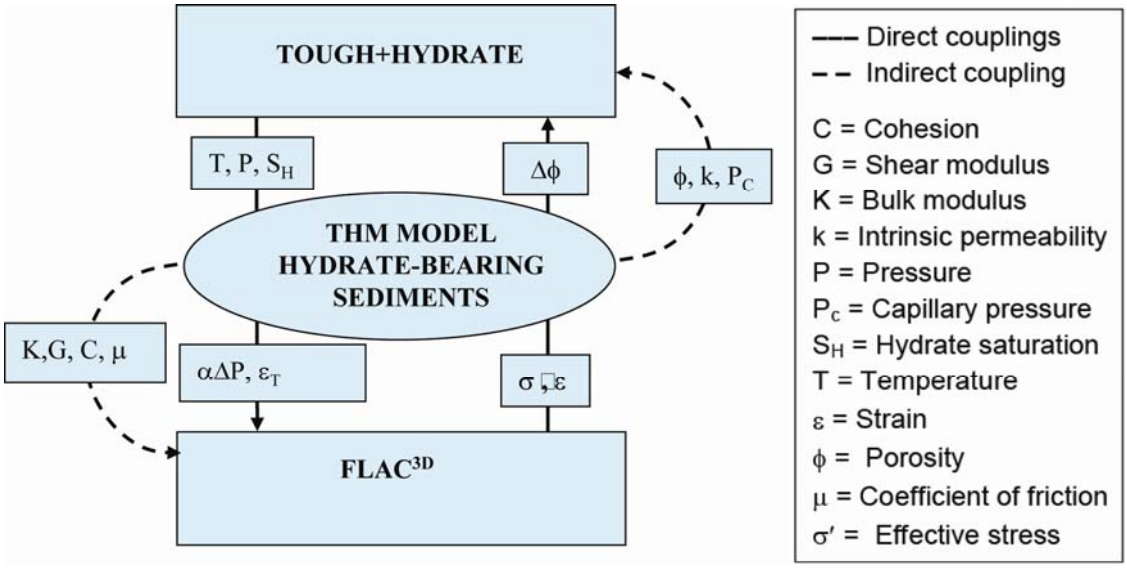

Figure 2 – Linking of TOUGH+HYDRATE with FLAC^{3D} for analysis of the HBS geomechanical behavior.

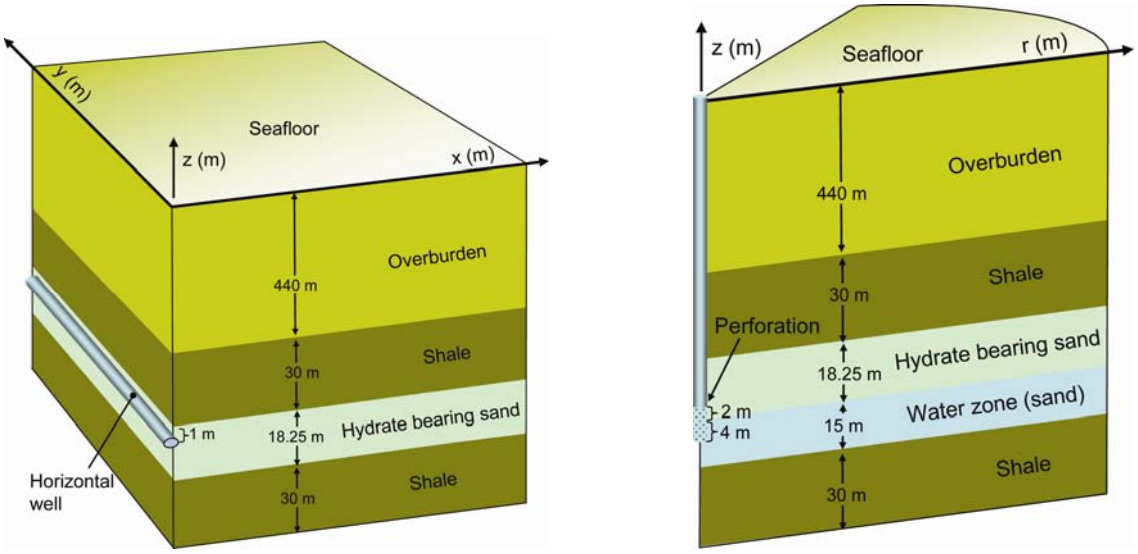

Figure 3 – Schematic of geometry for analysis of gas production from a deep oceanic HBS. (a) Case 1: Constant flowing bottom-hole pressure production from a Class 3 deposit using long-range horizontal wells. (b) Case 2: Constant rate production from a Class 2 deposit using vertical wells.

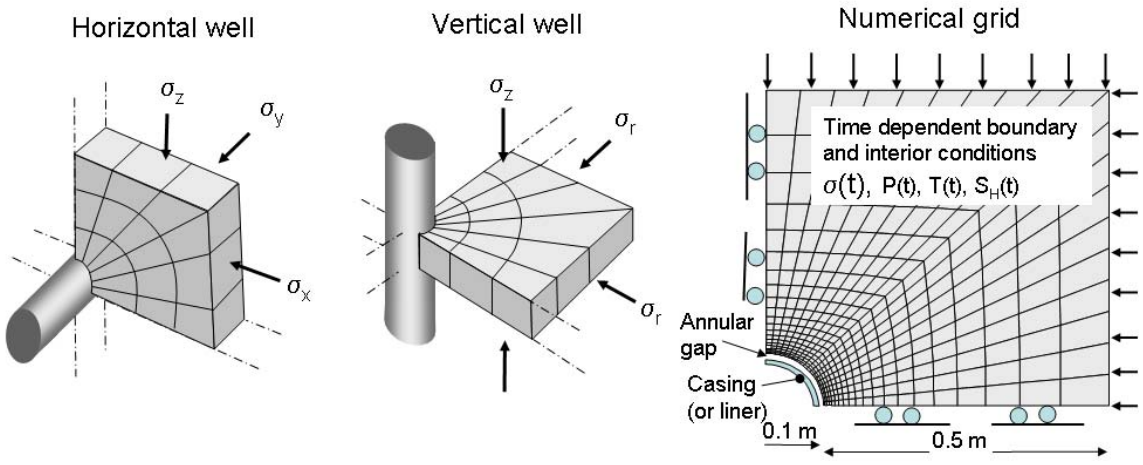

Figure 4 – Wellbore scale model domain for analysis of wellbore stability. Schematics of model domain and boundary stresses for modeling of a vertical well (left) and horizontal well (mid) and the numerical grid (right).

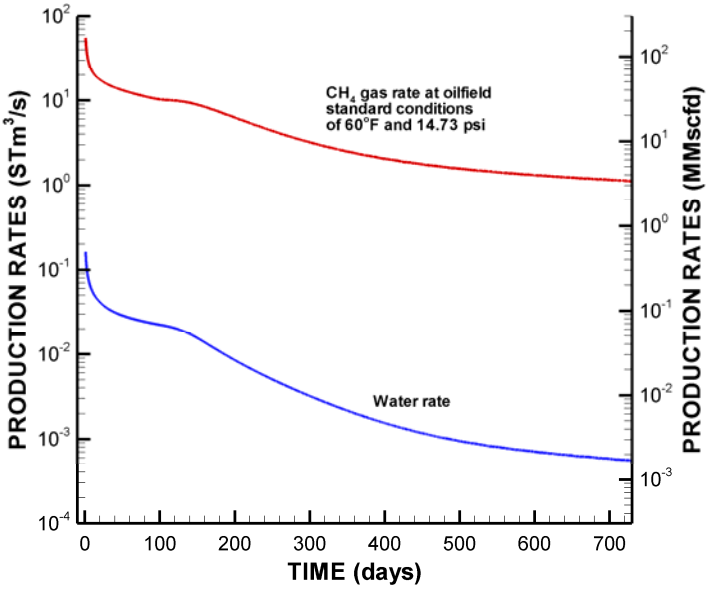

(a)

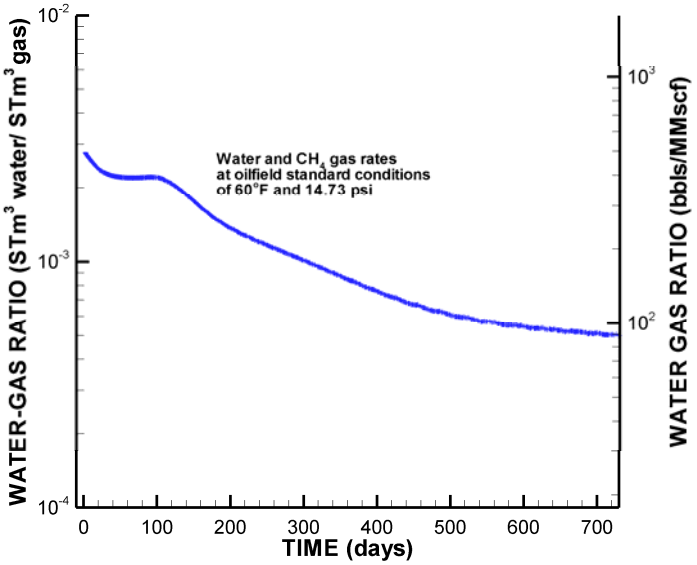

(b)

Figure 5 – Production rates for Case 1 (horizontal well): (a) CH_4 gas and water production rates, and (b) water-gas ratio.

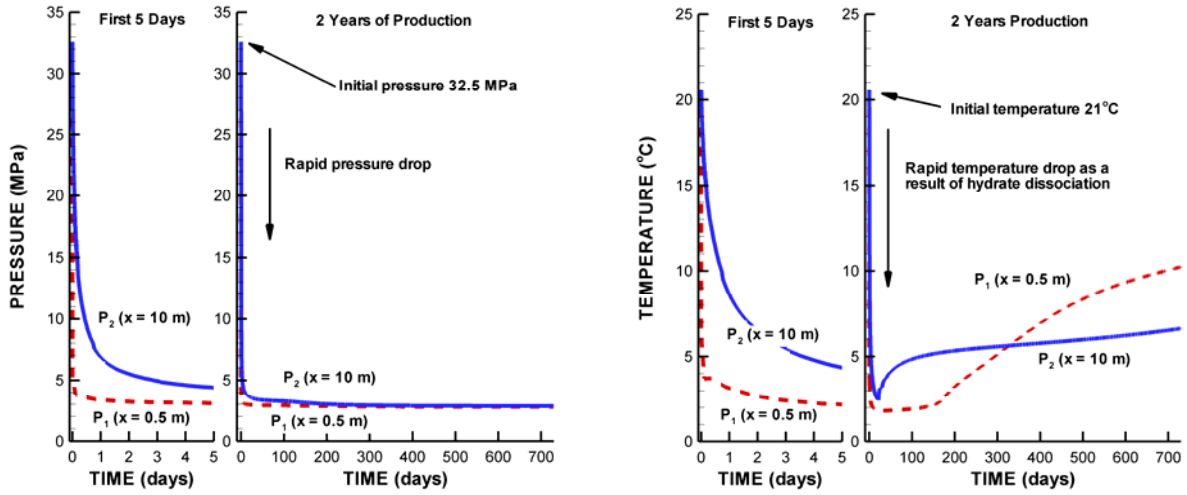

(a) (b)

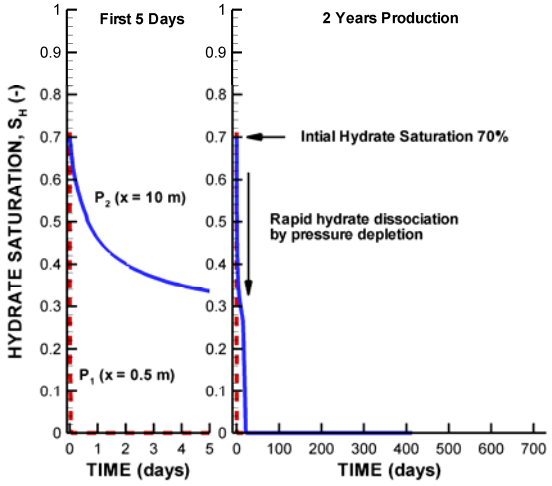

(c)

Figure 6 – Thermodynamic evolution at monitoring points P1 and P2 located (respectively) 0.5 and 10 m from the horizontal production well for Case 1 over 2 years of production: (a) pressure, (b) temperature, and (c) hydrate saturation.

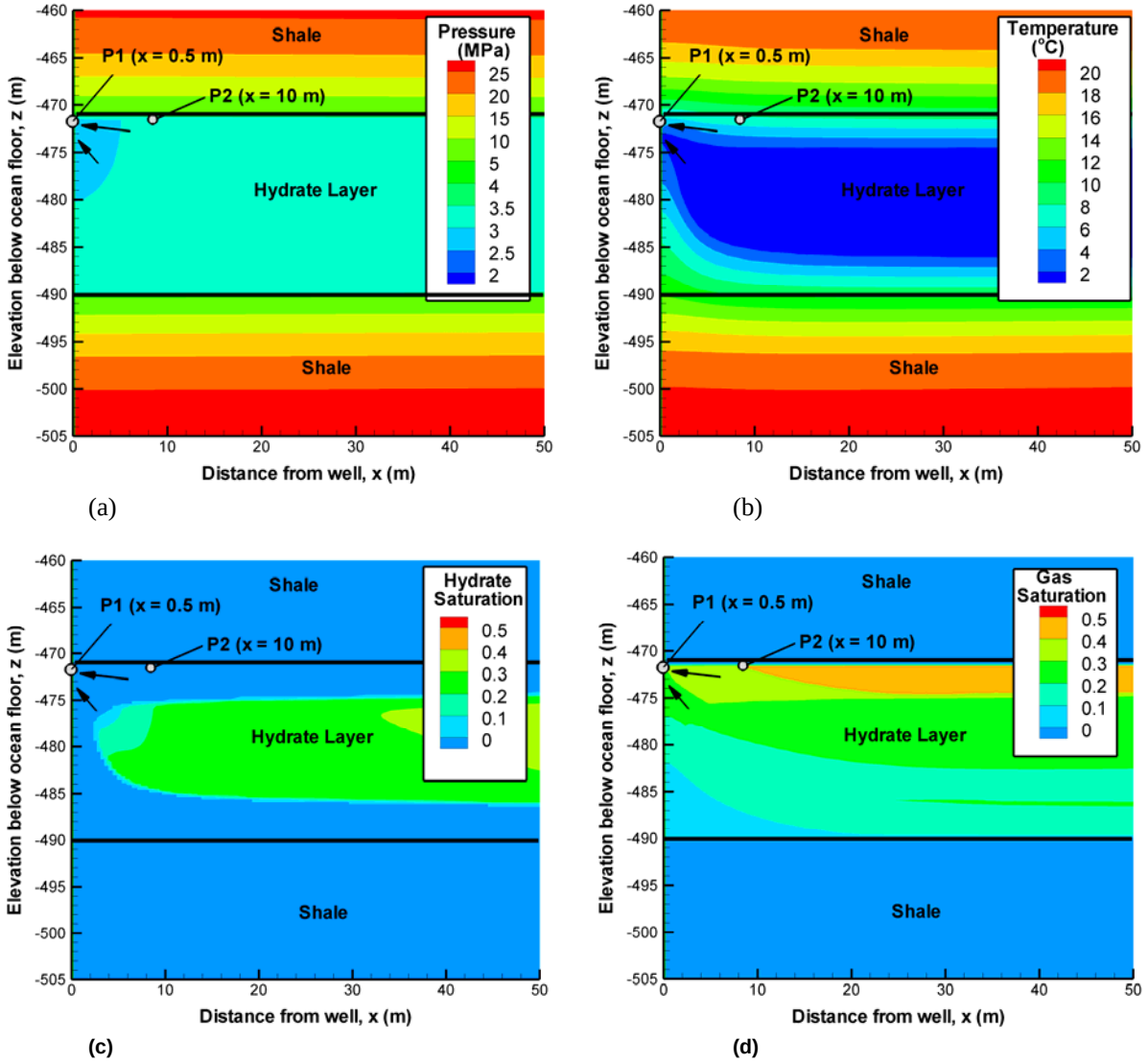

Figure 7 – Thermodynamic state after 6 months (180 days) of production for Case 1: (a) Pressure, (b) temperature, (c) hydrate saturation, and (d) gas (CH_4) saturation.

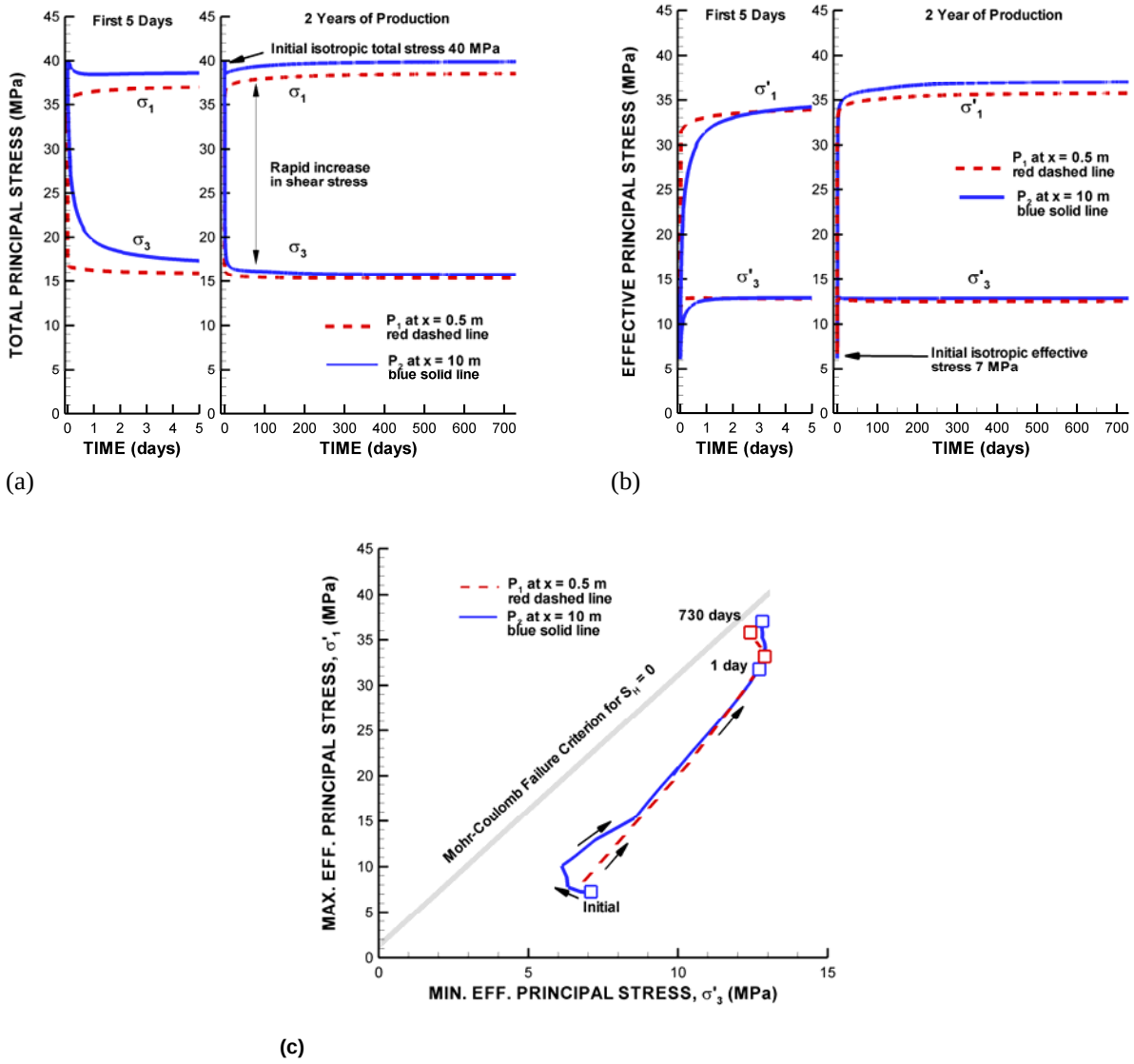

Figure 8 – Evolution of effective principal stresses for Case 1: (a) total principal stresses, (b) effective principal stresses, and (c) effective principal stress path with comparison to Mohr-Coulomb failure criterion.

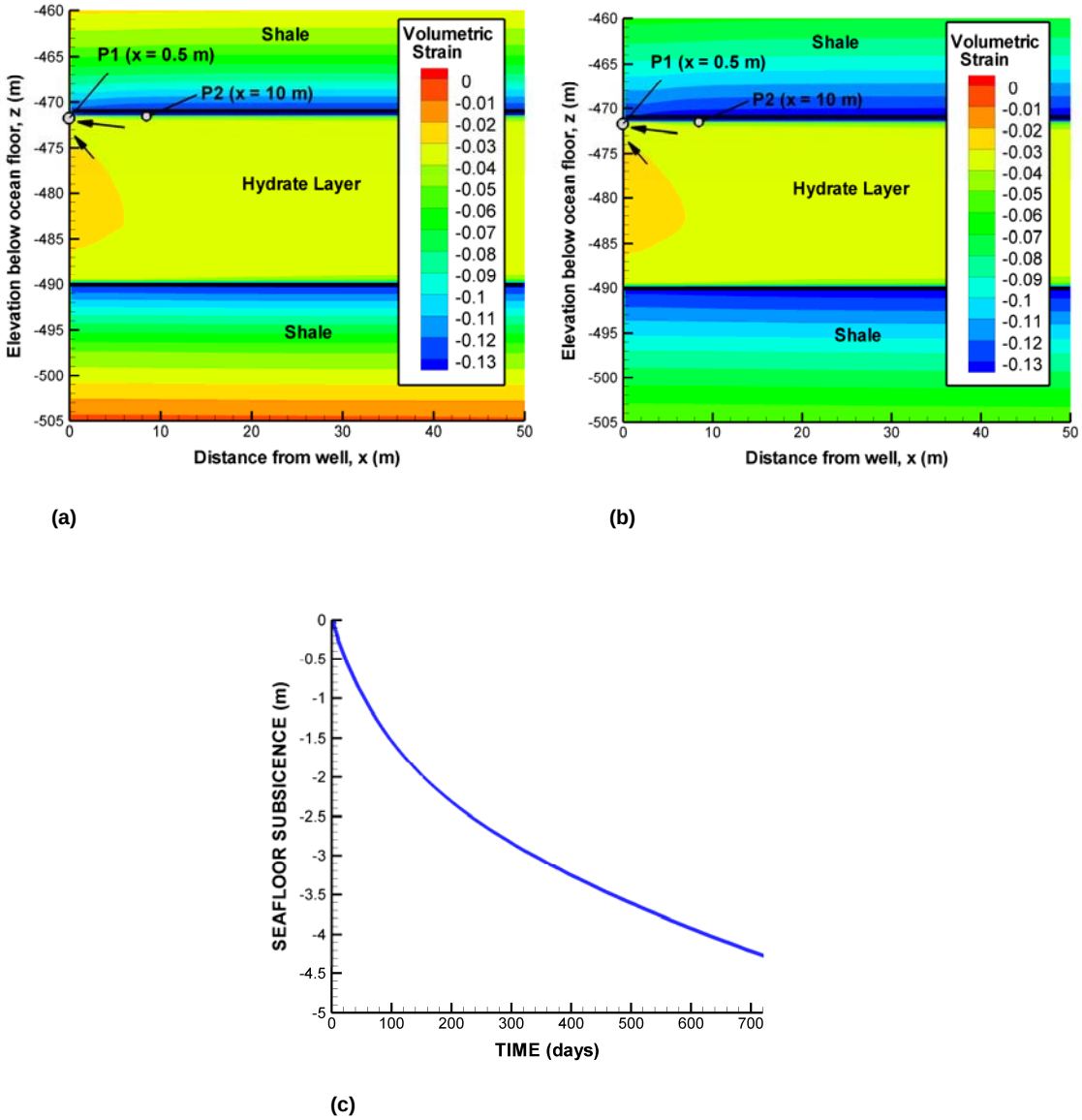

Figure 9 – Production-induced mechanical deformations for Case 1: (a) volumetric strain after 6 months (180 days), (b) volumetric strain after 2 years (720 days) of production, and (c) evolution of seafloor subsidence.

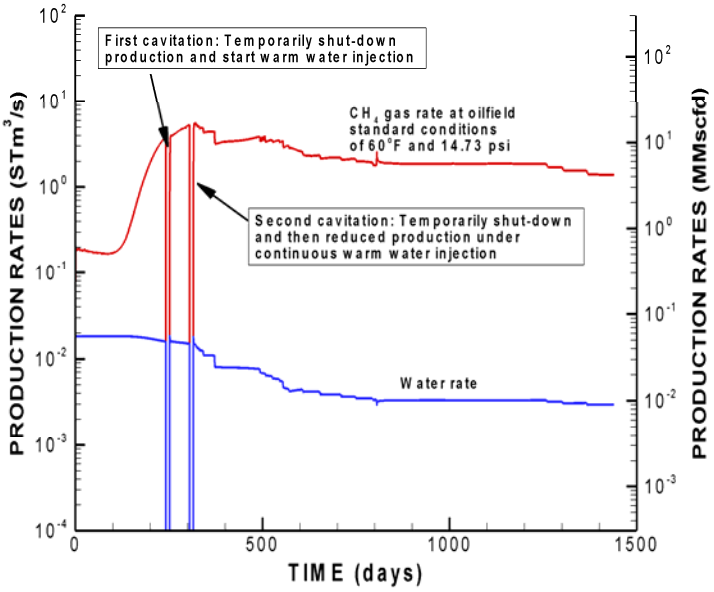

(a)

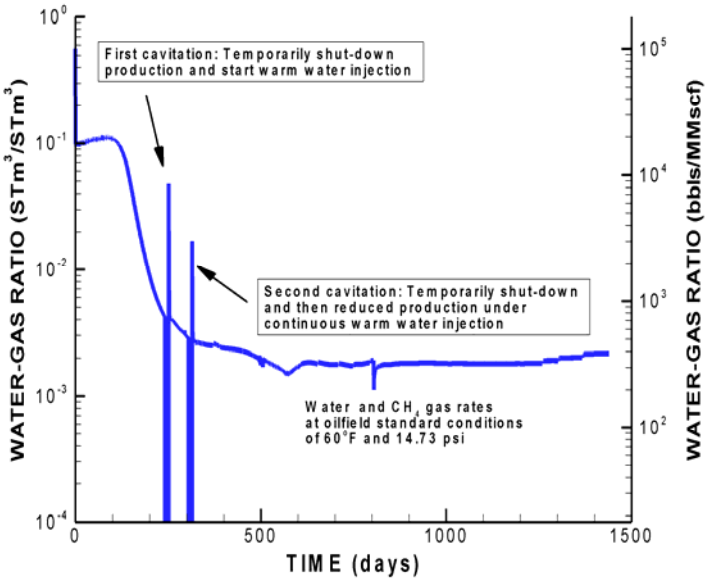

(b)

Figure 10 – Production rates for Case 2 (a) CH_4 gas and water production, and (b) water-gas ratio

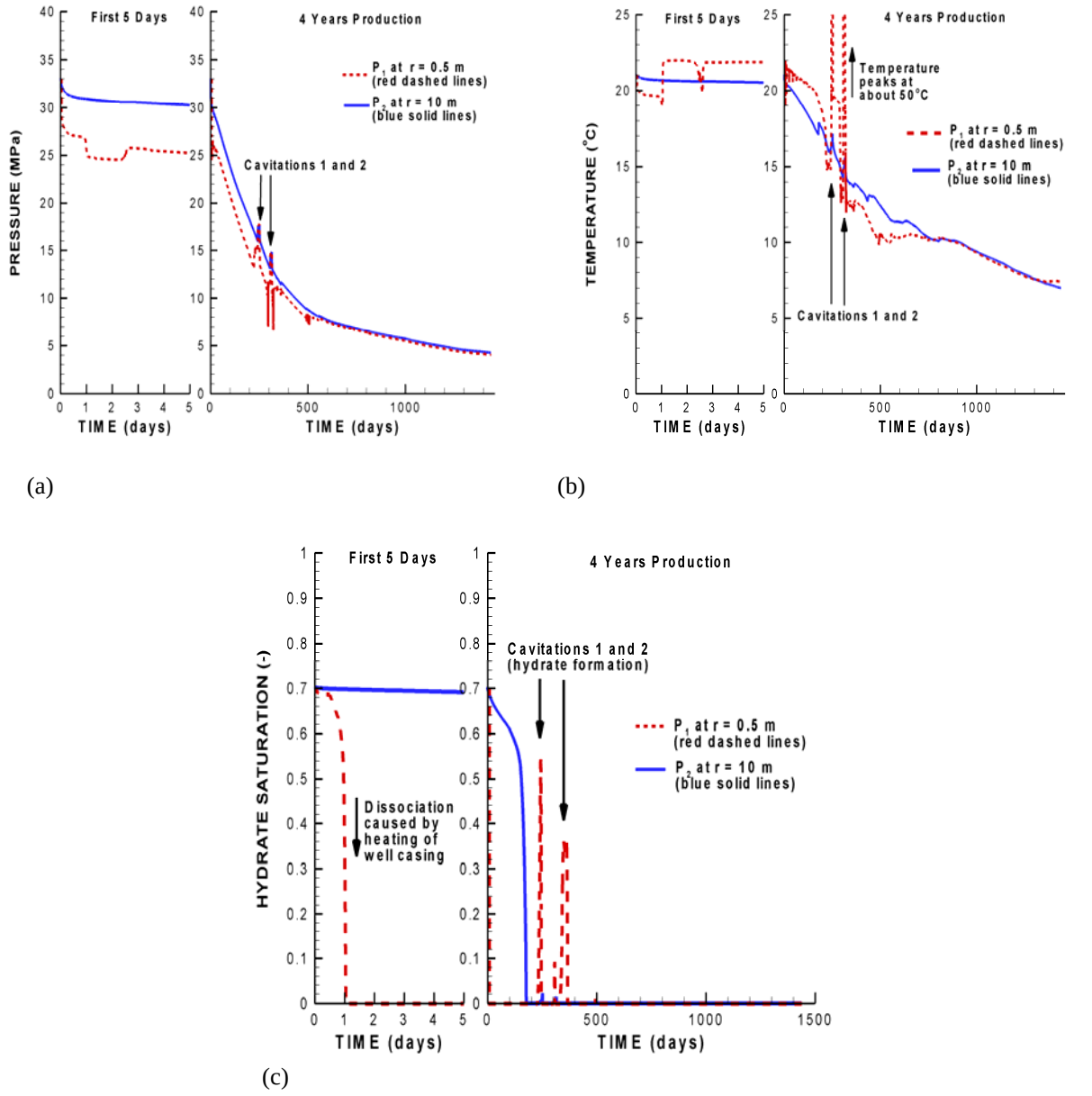

Figure 11 – Thermodynamic evolution at monitoring points P1 and P2 located (respectively) 0.5 and 10 m from the horizontal production well for Case 2 over 4 years of production: (a) pressure (b) temperature and (c) hydrate saturation.

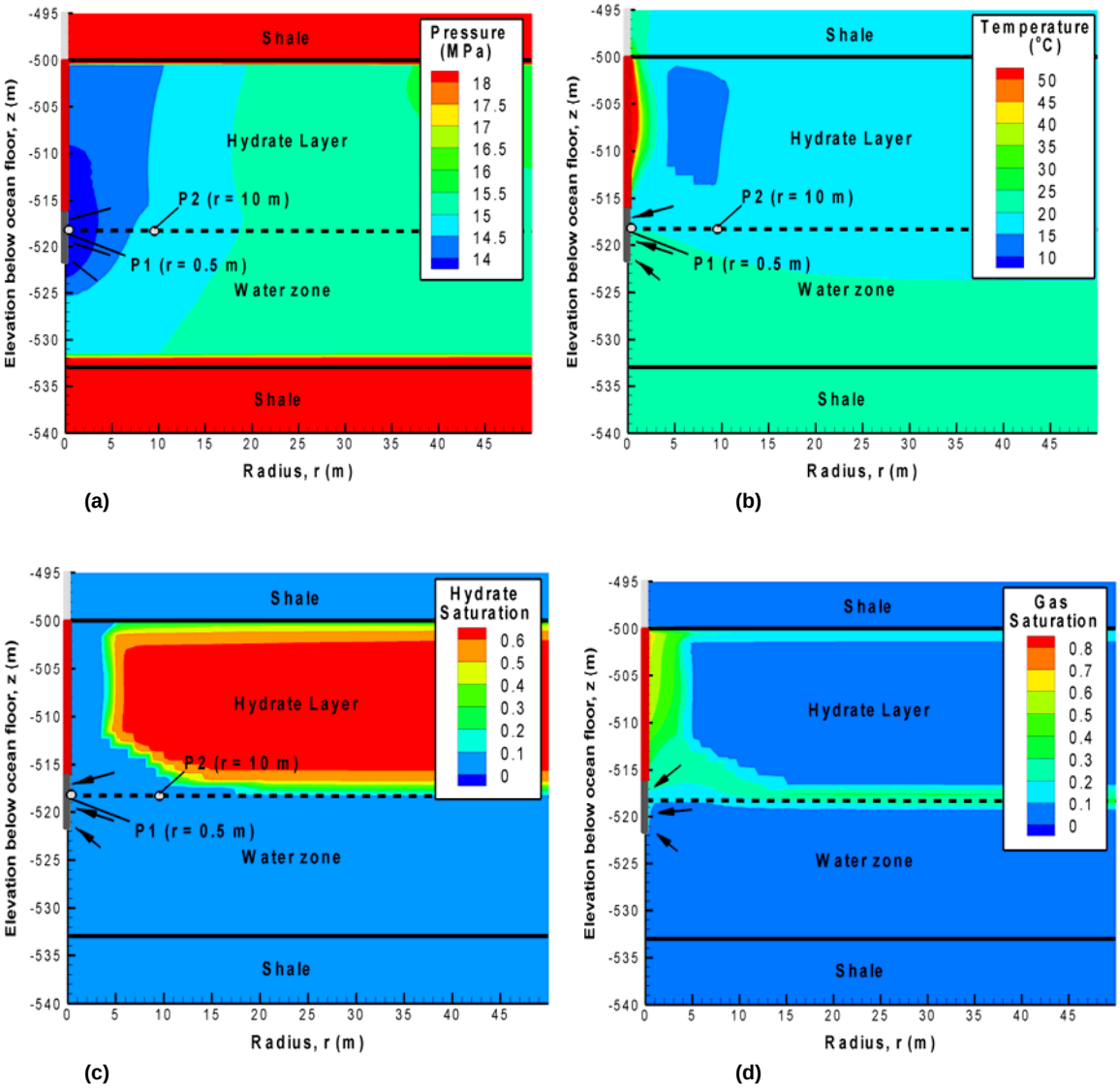

Figure 12 – Thermodynamic state after 6 months (180 days) of production for Case 2: (a) pressure, (b) temperature, (c) hydrate saturation, and (d) gas (CH_4) saturation.

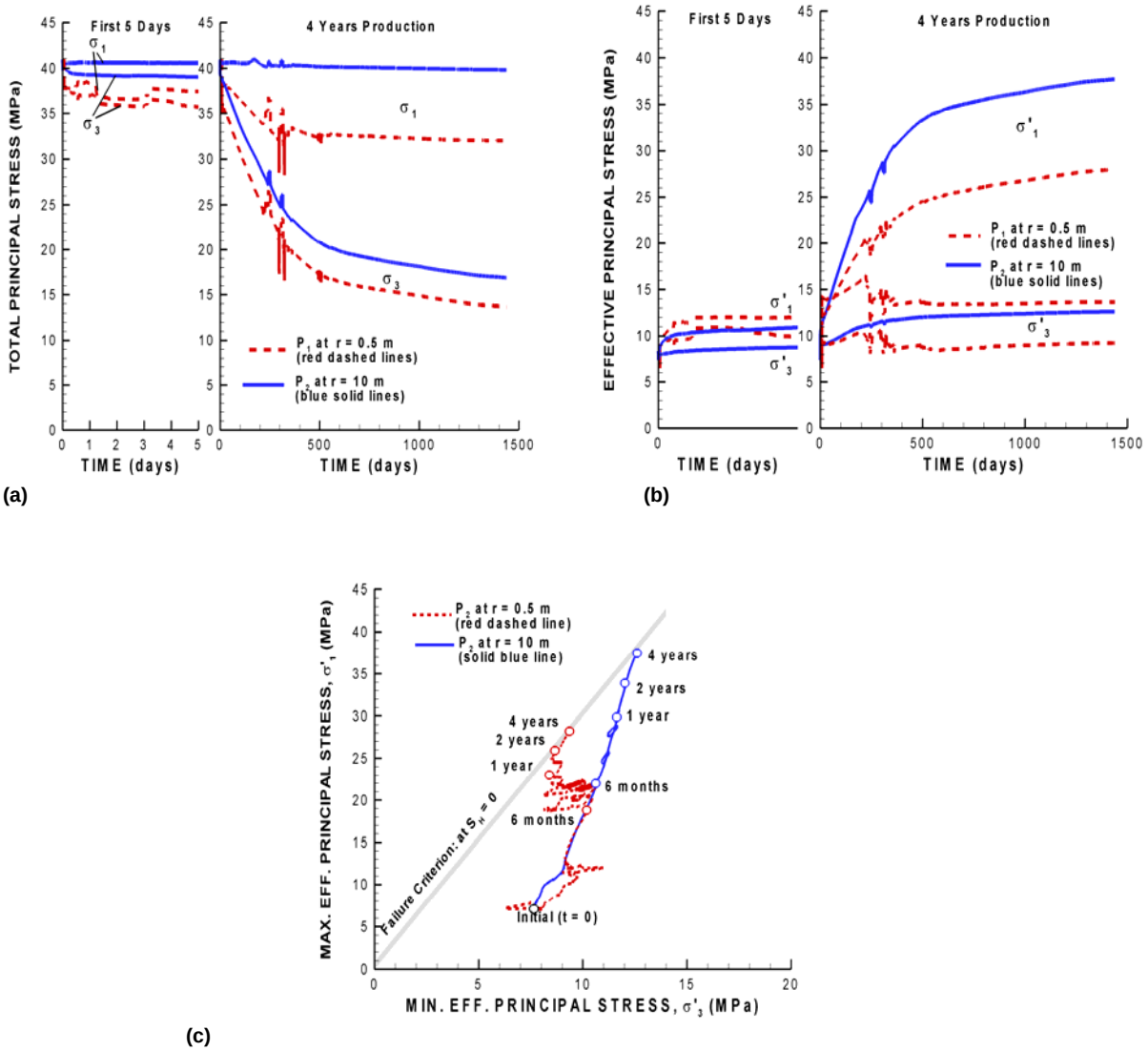

Figure 13 – Stress evolution for Case 2: (a) total principal stresses, (b) effective principal stresses, and (c) principal stress path with comparison to Mohr-Coulomb failure criterion.

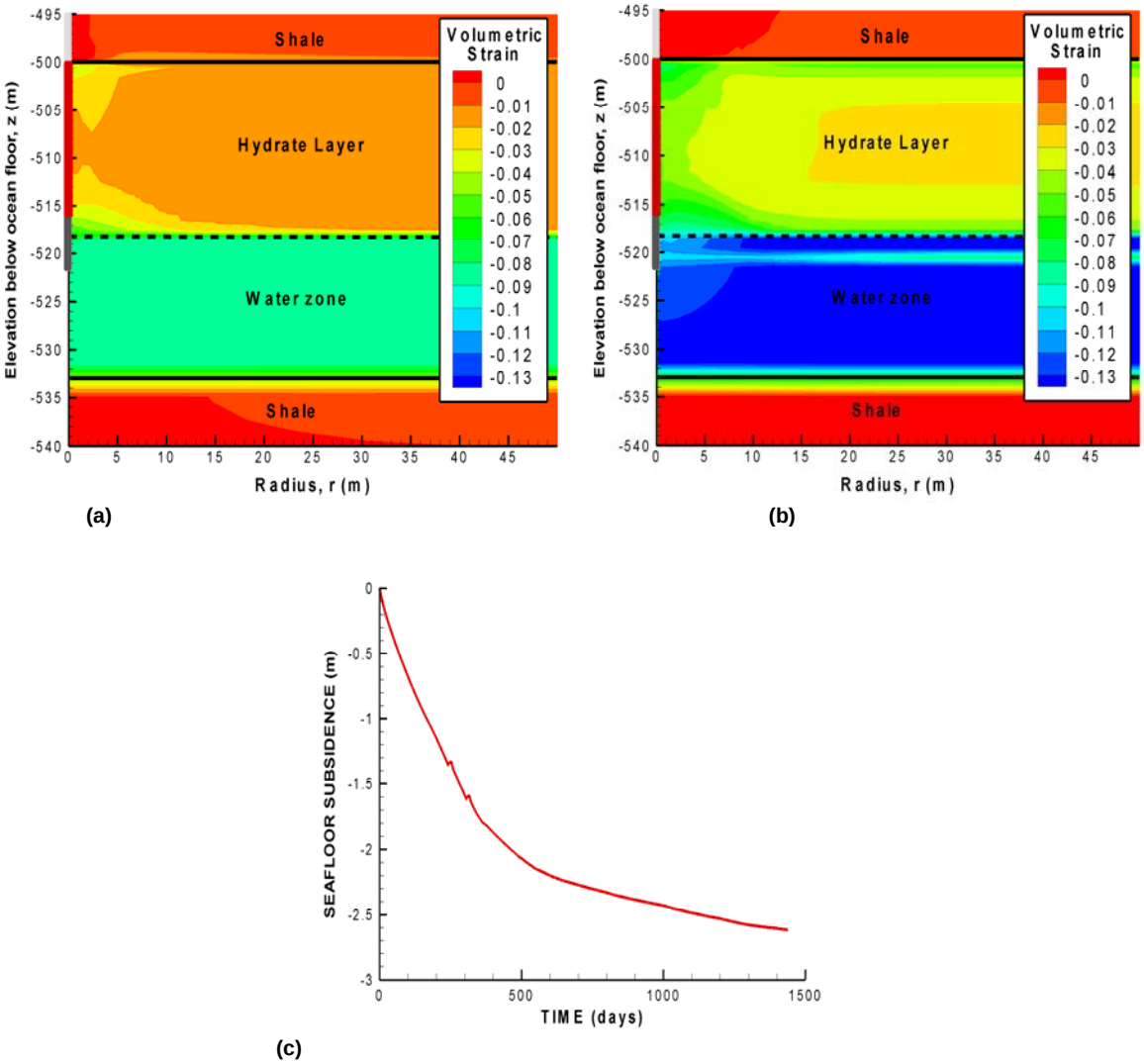

Figure 14 – Production-induced mechanical deformations for Case 2: Volumetric strain after (a) 6 months (180 days), and (b) 4 years (1460 days) of production and (c) evolution of seafloor subsidence.

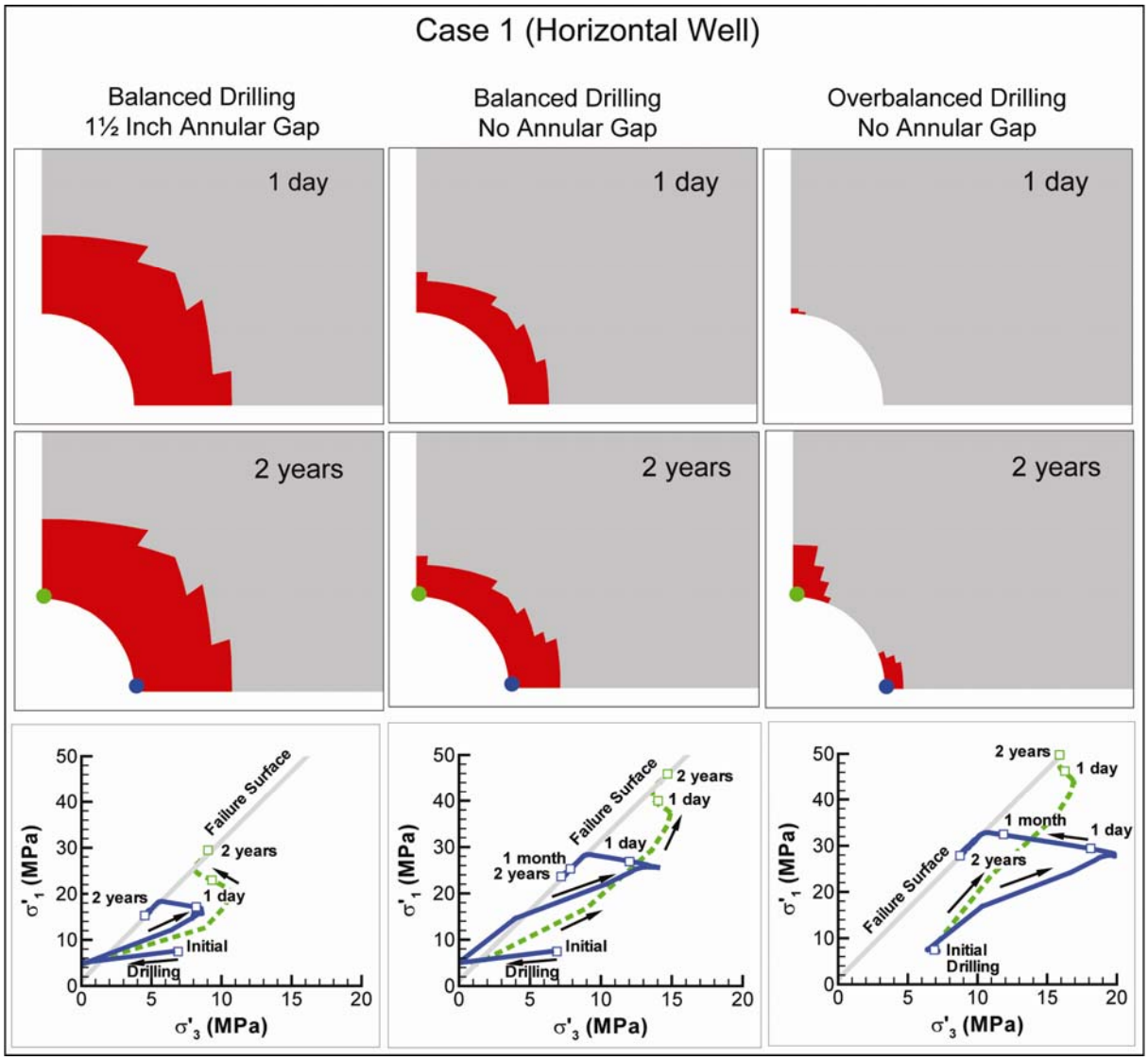

Figure 15 – Results of wellbore stability analysis for Case 1 considering three different sequences of drilling and completion: Distribution of the yield zone (red) after 1 day and 2 years of production, and the principal stress path at two points (blue and green) with comparison to Mohr-Coulomb failure surface for hydrate free conditions (S_H = 0). Note that the initial stress path appears to go above the failure surface for S_H = 0, because initially the shear strength is higher as a result of an initial hydrate saturation of 70% (S_H = 0.7).

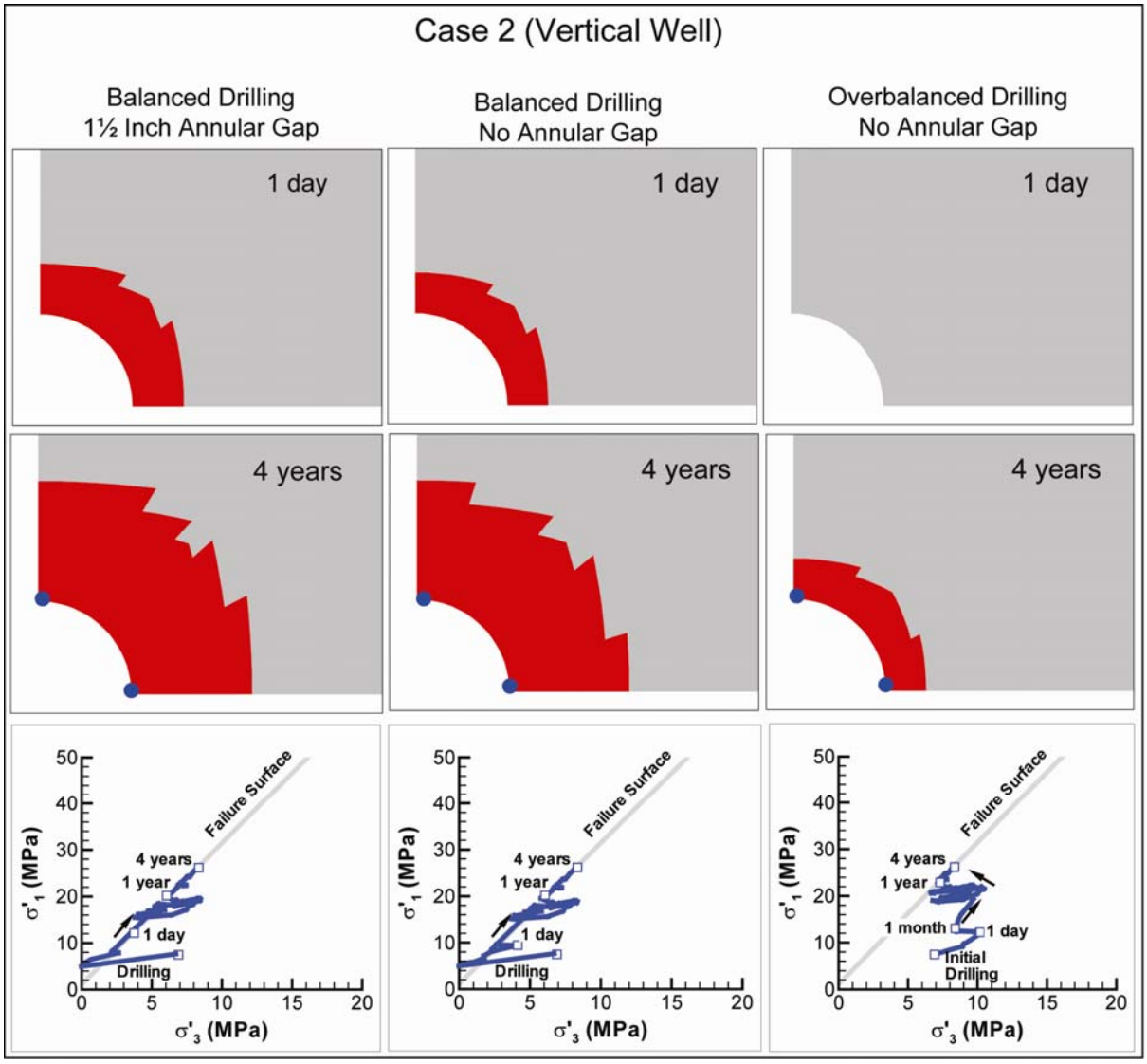

Figure 16 – Results of wellbore stability analysis for Case 2 considering three different sequences of drilling and completion: Distribution of the yield zone (red) after 1 day and 2 years of production and the principal stress path at two points (blue) with comparison to Mohr-Coulomb failure surface for hydrate free conditions (S_H = 0). The principal stress evolution is identical at the two blue points because of axisymmetric behavior and initial isotropic stress. Note that the initial stress path appears to go above the failure surface for S_H = 0, because initially the shear strength is higher as a result of an initial hydrate saturation of 70% (S_H = 0.7).

DISCLAIMER